Fast oxidation of sulfur dioxide by hydrogen peroxide in deliquesced aerosol particles

Tengyu Liu, Simon L. Clegg, Jonathan P.D. Abbatt

Version Post-print/Accepted Manuscript

Citation (published version) Liu, T., Clegg, S.L., Abbatt, J.P.D. 2020. Fast oxidation of sulfur dioxide by hydrogen peroxide in deliquesced aerosol particles. Proc. Natl. Acad. Sci. U.S.A. 117, 3, 1354-1359. https://doi.org/10.1073/pnas.1916401117.

Fast oxidation of sulfur dioxide by hydrogen peroxide in deliquesced aerosol particles

Tengyu Liu,[,1] Simon L. Clegg,[2] and Jonathan P. D. Abbatt*[,1]*

[1] Department of Chemistry, University of Toronto, Toronto, ON, M5S 3H6, Canada.

[2] School of Environmental Sciences, University of East Anglia, Norwich NR4 7TJ, U.K.

*email: tengyu.liu@utoronto.ca, jonathan.abbatt@utoronto.ca

Classification: PHYSICAL SCIENCES: Earth, Atmospheric, and Planetary Sciences

Abstract

Atmospheric sulfate aerosols have important impacts on air quality, climate, and human and ecosystem health. However, current air-quality models generally underestimate the rate of conversion of sulfur dioxide (SO_2) to sulfate during severe haze pollution events, indicating that our understanding of sulfate formation chemistry is incomplete. This may arise because the air-quality models rely upon kinetics studies of SO_2 oxidation conducted in dilute aqueous solutions, and not at the high solute strengths of atmospheric aerosol particles. Here, we utilize an aerosol flow reactor to perform direct investigation on the kinetics of aqueous oxidation of dissolved SO_2 by hydrogen peroxide (H_2O_2) using pH-buffered, submicrometer, deliquesced aerosol particles at relative humidity of 73 to 90%. We find that the high solute strength of the aerosol particles significantly enhances the sulfate formation rate for the H_2O_2 oxidation pathway compared to the dilute solution. By taking these effects into account, our results indicate that the oxidation of SO_2 by H_2O_2 in the liquid water present in atmospheric aerosol particles can contribute to the missing sulfate source during severe haze episodes.

Keywords: air pollution; Chinese haze; sulfate aerosol; sulfur dioxide oxidation; aerosol kinetics; multiphase chemistry

Significance

Atmospheric sulfate aerosol particles contribute significantly to poor air quality and direct forcing of the Earth's climate. However, air pollution and climate models simulate the formation of sulfate using acid rain chemistry known to be appropriate only for cloud water conditions. By measuring the oxidation of sulfur dioxide (SO_2) by hydrogen peroxide (H_2O_2) directly in hygroscopic, pH-buffered aerosol particles with high solute strength characteristic of many tropospheric conditions, we show that sulfate formation occurs significantly faster than under the cloudwater conditions previously explored. In part, ionic strength and general acid catalysis effects drive the fast chemistry. These results indicate that the H_2O_2-driven oxidation of SO_2 in aqueous aerosol particles can contribute to the missing sulfate source during severe haze pollution events.

Introduction

Sulfate aerosol is an important component of fine particulate matter that impacts air quality, climate, and human and ecosystem health (1-3). Atmospheric models currently generate aerosol sulfate either via condensation of H_2SO_4, which is formed via gas-phase oxidation of SO_2, or via a suite of oxidation processes involving SO_2 dissolved in cloudwater. Although the aerosol liquid water content (AWC) is generally much lower than cloud liquid water, it is possible that such aerosol multiphase oxidation processes may be important in polluted and high relative humidity conditions. However, it is uncertain whether the kinetics of aqueous oxidation of dissolved SO_2 by different oxidants investigated in bulk solution with low ionic strength (< 5 molal) are applicable to the high solute concentration situations that prevail for aerosol particles. Measuring the kinetics of aqueous oxidation of dissolved SO_2 in aerosol particles is thus critical to the accurate modeling of aerosol sulfate in the atmosphere.

Assessing the rate of aerosol sulfate formation in polluted conditions can evaluate the atmospheric importance of multiphase oxidation processes. In particular, rapid sulfate production has been observed during cloud-free, severe haze events in China, with the peak sulfate mass concentration reaching as high as ~ 300 $\mu g\ m^{-3}$ (4-8). However, current air-quality models that include gas-phase oxidation of SO_2 by the hydroxyl radical (9) and aqueous oxidation of dissolved SO_2 by hydrogen peroxide (H_2O_2) (10), O_3 (10), O_2 catalyzed by transition metal ions (TMI, i.e., Fe (III) and Mn (II)) (11-14), methyl hydrogen peroxide (15), and peroxyacetic acid (15) cannot capture these high levels of aerosol sulfate (5, 16, 17), indicating that our understanding of sulfate formation chemistry is fundamentally incomplete. Oxidation of dissolved SO_2 by NO_2 may be important if the aerosol pH is high (4, 6) and inclusion of a hypothetical heterogeneous oxidation process in aerosol particles can greatly improve the model performance (17). Overall, the formation mechanism of the missing sulfate source remains unclear and controversial (4, 6, 18-26).

Oxidation experiments with high solute strength aerosol face significant challenges due to the need for online measurement of the reaction kinetics using aerosol particles, and the necessity for good control of AWC and aerosol pH (27). Sulfate formation rates for many aqueous SO_2 oxidation pathways involving O_3, O_2+TMI, and NO_2 are strongly pH-dependent (6) and are subject to 1 to 2 orders of magnitude change if the pH changes by 1 unit because the solubility and effective Henry's law constant of SO_2 positively depend on pH (28). This sensitivity of sulfate formation rates to pH poses experimental challenges in controlling aerosol pH because product hydrogen ions (H^+) will perturb the aerosol pH. As an exception, the rate of aqueous oxidation of dissolved SO_2 by H_2O_2 is largely pH-independent for pH above 2 because the effects arising from the pH dependence of the SO_2 solubility and the reaction rate constant offset each other (10). This characteristic makes the SO_2-H_2O_2 reaction a useful system to isolate the effects of solute strength from aerosol pH on the sulfate formation rate.

Here, we study pH-buffered submicrometer, deliquesced aerosol particles in an aerosol flow tube to create high solute strengths, enabling direct investigation of the kinetics of aqueous oxidation of dissolved SO_2 by H_2O_2 in aerosol particles. Six types of seed aerosols were investigated, with aerosol pH buffered at 2.3 to 4.8 as calculated using the E-AIM model (29, 30) and a Pitzer activity coefficient model (31): A) a mixture of sodium chloride (NaCl)/malonic acid/sodium bimalonate (molar ratios 20:1:1, 6:1:1, 2:1:1 and aerosol pH 2.3–2.5), B) NaCl/sodium bimalonate/sodium malonate (molar ratios 20:1:1, 6:1:1, 2:1:1 and aerosol pH 4.8), C) sodium nitrate ($NaNO_3$)/malonic acid/sodium bimalonate (molar ratio 20:1:1 and aerosol pH 2.8), D) $NaNO_3$/sodium bimalonate/sodium malonate (molar ratio 20:1:1 and aerosol pH 4.0), E) malonic acid/sodium bimalonate (molar ratio of 1:1 and aerosol pH 2.8), and F) sodium bimalonate/sodium malonate (molar ratio of 1:1 and aerosol pH 3.9).

In part, the individual aerosol particles components were chosen to be representative of species found in the atmosphere. More importantly, they satisfy the demands of the experiment (see detailed explanation in *SI Appendix*, section S1) by providing different aerosol pH and different AWC (32), and by enabling explicit examination of the effects of aerosol pH and solute strength on the sulfate formation rate. Aerosol mass spectrometry (33) (AMS) quantitatively characterized the composition of seed aerosols and the sulfate that forms. A scanning mobility particle sizer (SMPS) was used to measure particle-size distributions and to determine the AWC. All experiments were performed at 21 to 25 ºC and high relative humidity (RH) (73 to 90%) to ensure that the seed aerosol particles are deliquesced; see Methods and *SI Appendix,* section S1 for details on the experimental conditions, choice of aerosol systems to study, instrument operation, and data analysis.

The overall goal of this work is to measure the sulfate formation rates on aerosol particles with high solute concentrations, to enable comparison with the literature parameters that have previously been obtained in bulk solutions. The results will provide an improved quantitative understanding of sulfate aerosol formation during severe haze pollution events.

Results

The kinetics of aqueous oxidation of dissolved SO_2 by H_2O_2 in a mixture of NaCl and malonic acid buffer aerosol particles (molar ratio of 20:1:1) at pH 2.5 are shown in Fig. 1. Results for the other aerosol types are qualitatively similar and shown in *SI Appendix* Fig. S3. The partial pressures of SO_2 and H_2O_2 were kept constant and in excess in each experiment so that the aerosol sulfate that forms is solely dependent on the reaction time. The dissolved sulfate concentrations, $[SO_4^{2-}]$ (molality units), show strong linear correlations ($r^2 > 0.96$) with the reaction time (Figs. 1A and C). As well, the slopes of the sulfate formation rate versus initial SO_2 and H_2O_2 concentrations using log-log plots (Figs. 1B and D) are close to unity (1.03 ± 0.14 and 1.19 ± 0.03, respectively), suggesting first-order reactions in dissolved SO_2 and H_2O_2. Except for some data points associated with the particles containing NaCl or $NaNO_3$, the estimated buffer capacity is higher than the amount of H^+ formed (see *SI Appendix,* section S1). It is possible that HCl or HNO_3 evaporate from the particles under those conditions, removing acidity. Nevertheless, the strong correlations in Fig. 1A and C show no signs of a slower reaction when a large amount of sulfate forms.

Overall, these observations are consistent with the assumed mechanism for the reaction (34):

$$HSO_3^- + H_2O_2 \rightleftharpoons HOOSO_2^- + H_2O \quad \text{(R1)}$$

$$\mathrm{HOOSO_2^- + H^+ \rightleftharpoons HOOSO_2H} \quad \text{(R2)}$$

$$\mathrm{HOOSO_2H \rightarrow 2H^+ + SO_4^{2-}} \quad \text{(R3)}$$

As well, it is known that weak acids, HX, can act as proton donors to promote the reaction through general acid catalysis:

$$\mathrm{HOOSO_2^- + HX \rightarrow 2H^+ + SO_4^{2-} + X^-} \quad \text{(R4)}$$

The overall rate expression (34, 35) valid for pH > 2 is:

$$\frac{\mathrm{dSO_4^{2-}}}{\mathrm{dt}} = (\mathrm{k} + \mathrm{k_{HX}}\,[\mathrm{HX}][\mathrm{H^+}]^{-1})\mathrm{K_{a1}H_{SO_2}P_{SO_2}H_{H_2O_2}P_{H_2O_2}} \quad (1)$$

where $k = k_{R3}K_{R1}K_{R2}$, and k_{R3} is a reaction rate coefficient, K_{R1} and K_{R2} are thermodynamic equilibrium constants, K_{a1} is the thermodynamic dissociation constant of H_2SO_3, and H_i and P_i represent the Henry's law constant and partial pressure of species i, respectively. k_{HX} is the overall rate constant for the general acid catalysis mechanism. We note that Eq. 1 is only applicable to ideal solutions. Known modifications to Eq. 1 for ionic strength effects are presented in *SI Appendix*, Table S4.

To convert the measured sulfate formation rate to units of $\mu g\ m^{-3}\ \cdot h^{-1}$, which are used for comparison to field measurements, the following equation was used:

$$\frac{\mathrm{dSO_4^{2-}}}{\mathrm{dt}}(\mu\mathrm{g\ m^{-3}h^{-1}}) = 3600\ \mathrm{s\ h^{-1}} \cdot 96\ \mathrm{g\ mol^{-1}} \cdot \frac{\mathrm{dSO_4^{2-}}}{\mathrm{dt}}(\mathrm{molal\ s^{-1}}) \cdot \frac{\mathrm{AWC}}{\rho_\mathrm{w}} \quad (2)$$

where AWC is in units of $mg\ m^{-3}$ and ρ_w is the water density in $kg\ L^{-1}$. Note that in previous studies (6, 19), an equivalent expression was employed with the sulfate formation rate in units of $M\ s^{-1}$. While this is appropriate for dilute conditions, for solutions with high ionic strength the aerosol liquid water volume is substantially smaller than the total aerosol volume and so Eq. 2 is more accurate. As a result, we determine the SO_2- and H_2O_2-dependent sulfate formation rates in molal s^{-1}, as illustrated by the slopes in Fig. 1A and C.

Fig. 2A and B show the ratio of the measured sulfate formation rates to the modeled ones for all six types of seed aerosol as a function of total solute concentration and ionic strength, respectively. Modeled sulfate formation rates were calculated based on the literature parameters of SO_2 oxidation by H_2O_2 obtained in bulk solutions, without taking the effects of ionic strength and general acid catalysis into account; see *SI Appendix*, section S2 for details. Overall, the measured sulfate formation rates are higher than the modeled values. For the mixed NaCl and malonic acid buffer aerosol particles with low ionic strengths ($I < 7$ molal) and low concentrations of malonic acid (< 0.6 molal) (Exp 1 through 7 and 12), the measured sulfate formation rates are $2.1 \pm 0.1 - 2.9 \pm 0.6$ times larger than the modeled ones. Overall, we conclude for these particles types that the pH does not affect the kinetics between pH values of 2.3 and 4.8. This is consistent with the bulk solution kinetics in the literature for solution pH values above 2.

For the more concentrated solutions ($I > 7$ molal), the ratio of the measured to the modeled sulfate formation rate displays strongly increasing trends with increasing malonic acid concentration and ionic strength as shown in Fig. 2B. The ratio is as high as 33 ± 4 to 51 ± 9 for the malonic acid buffer aerosol particles at pH 3.9 with ionic strength of around 14 molal. We believe there are at least 2 effects driving the increase: general acid catalysis by malonic acid and ionic strength effects. In addition, there is possibility of salting-in effects of SO_2 and H_2O_2 at high solute strengths, including the impact of high buffer concentrations, that are difficult to estimate.

To illustrate the general acid effects, the measured sulfate formation rate increases with malonic acid concentration for the mixed NaCl and malonic acid buffer aerosol particles at pH 2.3 to 2.4 at relatively constant ionic strengths of 3.9 and 6.6 molal (*SI Appendix*, Fig. S6 and Table S1, Exp# 13 through 18).

To isolate the ionic strength effect, it is necessary to account for the general acid catalyzed enhancement. To do this, we linearly fit the two k_{HX} reaction rate coefficients that we measured (*SI Appendix*, Fig. S6) as a function of ionic strength (*SI Appendix*, Fig. S7A), and use this fit to account for the general acid effect according to Eq. 1. The dependence of k_{HX} on ionic strength arises because k_{HX} is dependent on the pKa* of the general acid (*SI Appendix*, Fig. S7B) and the first pKa* of malonic acid depends on ionic strength (*SI Appendix*, Fig. S7C), where Ka* is the stoichiometric dissociation constant. From this analysis we conclude that the general acid catalysis effect on the systems with highest ionic strength (14 molal) is negligible and that the significant increase of the sulfate formation rate is largely due to the effect of ionic strength on the proton-catalyzed mechanism and, potentially, the salting-in of reactants as well. This is consistent with previous studies at lower ionic strengths (~5 molal NaCl) that have found enhancements in the proton-catalysis reaction rate coefficient k (34) and the Henry's law constant of H_2O_2 (36) (*SI Appendix*, Fig. S5). Referring to the reaction mechanism above, the strong dependence of the rate constant on ionic strength arises by lowering the stoichiometric dissociation constant of $HOOSO_2H$ (reverse of Reaction

R2) (34). In particular, at high ionic strength there will be less water to stabilize the ions into which $HOOSO_2H$ dissociates.

Relative to modeled rates in pure water, we plot the dependence of the enhancement factor of only the proton-catalyzed sulfate formation rate on ionic strength in Fig. 2C, i.e., the general acid catalyzed sulfate formation rate was subtracted from the measured sulfate formation rate to yield the proton-catalyzed sulfate formation rate (see details in *SI Appendix*, section S3). This factor reflects the overall effects of ionic strength on the reaction rate coefficient k, Henry's law constants of H_2O_2 and SO_2, and the first stoichiometric dissociation constant of H_2SO_3. We note that some data points are negative after correcting for the general acid effects. The enhancement factor is ~ 1.5 at ionic strengths of 2 to 6.5 molal. This is relatively good agreement given that we estimate that the uncertainties in our rates is on the order of a factor of two, when considering individual uncertainties in the kinetics plots, sulfate quantification, and determination of AWC. The enhancement factor increases to 33 ± 4 to 51 ± 9 at ionic strengths of 14 molal. For comparison, the modeled enhancement factors for ionic strength of 0 to 5 molal solutions were calculated using parameters obtained in bulk solutions (34, 36, 37); see *SI Appendix*, section S2 for details. The model results were also extrapolated to ionic strength of up to 43 molal using the functional formula derived in the past using much more dilute solutions. The high enhancement factors at high ionic strength ranges, which are within those (13 through 43 molal) of urban pollution episodes (6), indicate that ionic strength effects on the aqueous oxidation of SO_2 by H_2O_2 in aerosol particles should be considered in air quality models.

Discussion

By directly investigating the kinetics of aqueous oxidation of dissolved SO_2 by H_2O_2 in aerosol particles under well-controlled experimental conditions, we have examined solute strength effects on the sulfate formation rate. The major result is that there is an enhancement in the kinetics above the rate that prevails in dilute solutions typical of cloudwater. We believe that the enhancement effect is due to ionic strength effects and general acid catalysis arising from the malonic acid buffer, as well as potentially to salting-in of the reactants.

Overall, the rate of this multiphase reaction is driven by the volume of liquid water present. When clouds are present, the liquid water content is many orders of magnitude higher than in aerosol particles, even for highly polluted conditions. Under such conditions, SO_2 oxidation will proceed preferentially in the cloud droplets. Similarly, this aerosol multiphase reaction is unlikely to be important in clean conditions when the aerosol liquid water content is very low. However, it has the potential to have atmospheric importance under polluted conditions.

To illustrate, Fig. 3 shows the steady-state sulfate formation rates by aqueous SO_2 oxidation through different reaction pathways in aerosol particles following the approach of Cheng et al. (6). According to their work and that of Zheng et al. (17), a missing sulfate source of anywhere from 0.3 to 5 $\mu g\ m^{-3} \cdot h^{-1}$, depending on the $PM_{2.5}$ level, is needed to explain the sulfate formation during haze episodes in Beijing in January 2013 (see figure 3 of ref. (6)). Based on this model (6), the NO_2 reaction pathway may be the missing sulfate source if the aerosol pH is above 6 while the TMI reaction pathway will dominate sulfate formation if the aerosol pH is below 4.5. However, ionic strength effects on sulfate formation rate were not taken into account in the model of Cheng et al. (6).

By incorporating the enhancement factors of sulfate formation rate at high ionic strength (around 14 molal) into the model, the sulfate formation rate for the H_2O_2 reaction pathway increases from ~0.07 μg m^{-3} h^{-1} to 2.3–3.6 μg m^{-3} h^{-1}. Recently, Ye et al. (18) have reported that H_2O_2 concentrations during Beijing haze events were more than 1 order of magnitude higher than the value (0.01 ppb) assumed in the model of Cheng et al. (6). By updating the model with a H_2O_2 concentration of 0.1 ppb, the sulfate formation rate for the H_2O_2 reaction pathway increases to 23.2–36.0 μg m^{-3} h^{-1}.

We also investigated the effects of ionic strength on the aqueous TMI-catalyzed oxidation rate of dissolved SO_2 by O_2 in aerosol particles. We find that the sulfate formation rate is slower by a factor of ~ 85 at an ionic strength of 2.8 molal compared to that in dilute solution; see *SI Appendix*, section S4 for details. By taking the impact of ionic strength on the TMI reaction pathway into consideration, we find that the sulfate formation rate for the H_2O_2 reaction pathway is larger than all other reaction pathways for aerosol pH levels up to 6.2. This pH value exceeds the reported aerosol pH values (4 to 5) during severe haze episodes in northern China (see ref. (38) and references therein). As the sulfate formation rate for the H_2O_2 reaction pathway is independent of aerosol pH for pH levels above 2, the sulfate formation can be maintained at a high rate even when the aerosol particles become more acidic.

These results draw attention to the rates of formation of H_2O_2 that are required to sustain the aerosol-mediated SO_2 oxidation. To our knowledge, the mixing ratio of H_2O_2 was not measured for the January 2013 severe haze conditions presented in Fig. 3 (6). Modeling of H_2O_2 measurements in Beijing during March 2016 was consistent with a production rate of 0.5 ppbv d^{-1}, with more H_2O_2 formed via alkene ozonolysis than via the HO_2 self-reaction (39). Assuming that H_2O_2 production limits the rate of sulfate formation, this H_2O_2 production rate can account for up to 20% of the missing sulfate source in the January 2013 case and roughly 1/3 of the sulfate formed in January and February 2015 reported by Wang et al. (4). These estimates are highly uncertain, however, being dependent on the photochemical conditions that give rise to H_2O_2.

Our results highlight the important role of high solute strength in sulfate formation in deliquesced aerosol particles. Specifically, there is the need for an improved understanding on the role of ionic strength effects on atmospheric aqueous multiphase chemistry, as pointed out by a recent review of the field of laboratory atmospheric chemistry (40). As well, the importance of general acid catalysis needs to be considered not only for the many organic acids that are present under pollution conditions but potentially also for ammonium ions which are present in aerosol particles at very high concentrations. While such rate enhancements may arise under any conditions with a high aerosol liquid water content and solute concentrations, for the specific Chinese haze situation it is particularly important to assess these effects on the reactions of organic hydroperoxides, NO_2 and O_3 that also oxidize dissolved SO_2 (41), over a range of aerosol pH. This will permit a more comprehensive assessment of the overall rate of multiphase sulfur oxidation under cloud-free conditions.

Methods

Aerosol particle generation. Our goal was to investigate the kinetics of aqueous oxidation of dissolved SO_2 by H_2O_2 in high solute strength aerosol particles, achieved by generating pH-buffered polydisperse deliquesced aerosol particles using a constant output atomizer (TSI 3076) from the following solutions: A) a mixture of NaCl/malonic acid/sodium bimalonate (10/0.5/0.5 mM, 3/0.5/0.5 mM, and 1/0.5/0.5 mM); B) NaCl/sodium bimalonate/sodium malonate (10/0.5/0.5 mM, 3/0.5/0.5 mM, and 1/0.5/0.5 mM); C) $NaNO_3$/malonic acid/sodium bimalonate (10/0.5/0.5 mM); D) $NaNO_3$/sodium bimalonate/sodium malonate (10/0.5/0.5 mM); E) malonic acid/sodium bimalonate (5/5 mM); and F) sodium bimalonate/sodium malonate (5/5 mM). A small fraction of the humidified aerosol flow from the atomizer was mixed with a humidified N_2 flow and entered the kinetics flow tube, resulting in high relative humidity (73-90%) to ensure that the seed aerosol particles are deliquesced and maintain enough aerosol liquid water to enable aqueous oxidation. Additional details on generating seed aerosols are provided in *SI Appendix*, section S1.

Flow tube experiments. A schematic of the full experimental setup is shown in *SI Appendix*, Fig. S1. All experiments were conducted in a vertically oriented pyrex flow tube (length 95 cm, inner diameter 6.2 cm) at a total flow rate of 1500 sccm at laminar flow conditions (Reynolds Number ~34), in which constant flows of SO_2 (10, 25, or 50 sccm carrier gas), gas phase H_2O_2 (10 or 20 sccm carrier gas), and aerosol particles were well mixed. Gas-phase H_2O_2 was generated by bubbling N_2 through an aqueous H_2O_2 solution (15% or 30% by weight) and injected into the central portion of the humidified aerosol flow by a movable stainless-steel injector tube that is inserted axially down the center of the flow tube, enabling variable reaction time in a step-wise manner. In each experiment, the aerosol particles were first characterized in the presence of SO_2 and absence of H_2O_2 to quantify the background sulfate concentrations. Then the aqueous oxidation of SO_2 was initiated by introducing H_2O_2. Before entering the instruments for aerosol composition characterization, the aerosol particles alternatively passed through or bypassed a diffusion dryer to remove or sustain aerosol water. Experiments with different initial concentrations of SO_2 and H_2O_2 as well as seed aerosol types were carried out at 21 to 25 ºC and high relative humidity (73 to 90%). All reported sulfate concentrations were corrected for the background sulfate concentrations. Details of the experimental setup and procedure are provided in *SI Appendix*, section S1.

Measurements. Both compact and high-resolution time-of-flight aerosol mass spectrometers (33) (C-ToF-AMS and HR-ToF-AMS; Aerodyne Research) were deployed to characterize the concentration and chemical composition of aerosol particles. Prior to the experiments, the ionization efficiency (IE) of the AMS was calibrated using 300 nm ammonium nitrate particles. The sulfate was measured in the form of sodium sulfate because the sulfuric acid that was generated in the reaction was buffered by sodium bimalonate or sodium malonate. Therefore, a sulfate fragmentation table without water fragments was used (42). The relative ionization efficiency (RIE) of sulfate was determined for sodium sulfate to be 0.12 and 0.24 for the C-ToF-AMS and HR-ToF-AMS, respectively, and applied to the quantification of sulfate concentrations. The difference between sulfate concentrations simultaneously measured by these two AMS was within 10%. A collection efficiency of unity was assumed for the deliquesced aerosol particles (43). An SMPS (TSI) was used to measure the particle size distributions. Gas-phase monitors were used to measure SO_2 (Model 43i; Thermo) and H_2O_2 (PI2114; PICARRO) gas-phase mixing ratios. Details regarding the comprehensive calibration and operation of the AMS are described in *SI Appendix*, section S1.

Calculation of aerosol pH, sulfate molality and ionic strength. The relative concentrations of the solutes in the aerosol particles were assumed to be the same as in the solution in the atomizer with no fractionation, resulting in aerosol particles pH buffered at 2.3 to 4.8, estimated using the E-AIM model (29, 30) and a Pitzer activity coefficient model (31). Here, pH is defined as the negative logarithm with base 10 of the molality-based H^+ activity.

$$\mathrm{pH} = -\log_{10}(\gamma_{\mathrm{H^+}} m_{\mathrm{H^+}}) \quad (3)$$

where γ_{H^+} and m_{H^+} represent the molality-based activity coefficient and molality of H^+, respectively. For the mixture of NaCl and organic buffer, the molalities of all ions and neutral species were first estimated using the E-AIM model which were then input to the Pitzer model to calculate the equilibrium speciation to determine the aerosol pH. Given that the Pitzer model is developed for systems with NaCl and relatively low concentrations of malonic acid species, the aerosol pH for other systems (i.e. with no NaCl present) was estimated using the E-AIM model only. For comparison, the Pitzer model gave approximately 0.4 unit lower pH values for the mixture of NaCl/malonic acid/sodium bimalonate and 1 unit higher pH values for the mixture of NaCl/sodium bimalonate/sodium malonate compared to the E-AIM model results (*SI Appendix*, Fig. S9). We note that 1 unit difference of pH will not impact our conclusions given that the enhancement factors for the proton-catalyzed sulfate formation rate at the highest ionic strength (~14 molal) are pH-independent (*SI Appendix*, section S5 and Fig. S10A).

The sulfate molality was calculated from the sulfate concentrations (μg m^{-3}) and aerosol liquid water volume, which was determined as the volume difference between the deliquesced and effloresced aerosol particles bypassing or passing through the diffusion dryer. We note that there is an inherent assumption that the molar volumes of the solutes are the same in the dry and wet cases. For comparison, the aerosol liquid water volume was also determined by multiplying the total measured aerosol volume by the ratio of the aerosol liquid water volume to the total aerosol volume estimated using the E-AIM model, resulting in an enhancement factor of 19 ± 3 to 30 ± 5 for the proton-catalyzed sulfate formation rate at ionic strengths of 14 molal (*SI Appendix*, section S5 and Fig. S10B). This does not impact our conclusion that the oxidation of SO_2 by H_2O_2 in aerosol particles can contribute to the missing sulfate source during severe haze episodes.

The ionic strength was calculated via the following equation:

$$I = \frac{1}{2}\sum m_i\, z_i^2 \tag{4}$$

where m_i and z_i represent the molality of each ion and its corresponding charge, respectively. The ionic strength was estimated using the E-AIM model (29) assuming the relative composition of the aerosol particles to be the same as in the solution (*SI Appendix*, Table S1).

Data availability. All data are available from the corresponding author on request.

Acknowledgments

The authors thank the Natural Sciences and Engineering Research Council for funding, and Prof. T. Kahan for the loan of the PICARRO analyzer.

Author contributions

T.L. and J.A. designed the research project; T.L. performed the research; T.L., S.C., and J.A. analyzed data and T.L. and J.A. wrote the paper.

Competing interests

The authors declare no competing interests.

References

1. D. A. Grantz, J. H. B. Garner, D. W. Johnson, Ecological effects of particulate matter. *Environ. Int.* **29**, 213-239 (2003).
2. S. Fuzzi *et al.*, Particulate matter, air quality and climate: lessons learned and future needs. *Atmos. Chem. Phys.* **15**, 8217-8299 (2015).
3. A. Nel, Air Pollution-Related Illness: Effects of Particles. *Science* **308**, 804-806 (2005).
4. G. Wang *et al.*, Persistent sulfate formation from London Fog to Chinese haze. *Proc. Natl. Acad. Sci.* **113**, 13630-13635 (2016).
5. Y. Wang *et al.*, Enhanced sulfate formation during China's severe winter haze episode in January 2013 missing from current models. *J. Geophys. Res.-Atmos.* 10.1002/2013JD021426, 2013JD021426 (2014).
6. Y. Cheng *et al.*, Reactive nitrogen chemistry in aerosol water as a source of sulfate during haze events in China. *Sci. Adv.* **2** (2016).
7. R.-J. Huang *et al.*, High secondary aerosol contribution to particulate pollution during haze events in China. *Nature* **514**, 218 (2014).
8. S. Guo *et al.*, Elucidating severe urban haze formation in China. *Proc. Natl. Acad. Sci.* **111**, 17373-17378 (2014).
9. J. G. Calvert, F. Su, J. W. Bottenheim, O. P. Strausz, Mechanism of the homogeneous oxidation of sulfur dioxide in the troposphere. *Atmos. Environ.* **12**, 197-226 (1978).
10. M. R. Hoffmann, J. G. Calvert, Chemical Transformation Modules for Eulerian Acid Deposition Models: Volume II, the Aqueous-phase Chemistry. *EPA/600/3-85* **17** (1985).
11. T. Ibusuki, K. Takeuchi, Sulfur dioxide oxidation by oxygen catalyzed by mixtures of manganese(II) and iron(III) in aqueous solutions at environmental reaction conditions. *Atmos. Environ.* **21**, 1555-1560 (1987).
12. L. R. Martin, T. W. Good, Catalyzed oxidation of sulfur dioxide in solution: The iron-manganese synergism. *Atmos. Environ.* **25**, 2395-2399 (1991).
13. B. Alexander, R. J. Park, D. J. Jacob, S. Gong, Transition metal-catalyzed oxidation of atmospheric sulfur: Global implications for the sulfur budget. *J. Geophys. Res.-Atmos.* **114** (2009).
14. E. Harris *et al.*, Enhanced Role of Transition Metal Ion Catalysis During In-Cloud Oxidation of SO2. *Science* **340**, 727-730 (2013).
15. C. J. Walcek, G. R. Taylor, A Theoretical Method for Computing Vertical Distributions of Acidity and Sulfate Production within Cumulus Clouds. *J. Atmos. Sci.* **43**, 339-355 (1986).
16. R. Zhang *et al.*, Formation of Urban Fine Particulate Matter. *Chem. Rev.* **115**, 3803-3855 (2015).
17. B. Zheng *et al.*, Heterogeneous chemistry: a mechanism missing in current models to explain secondary inorganic aerosol formation during the January 2013 haze episode in North China. *Atmos. Chem. Phys.* **15**, 2031-2049 (2015).
18. C. Ye *et al.*, High H2O2 Concentrations Observed during Haze Periods during the Winter in Beijing: Importance of H2O2 Oxidation in Sulfate Formation. *Environ. Sci. Technol. Lett.* **5**, 757-763 (2018).
19. P. He *et al.*, Isotopic constraints on heterogeneous sulfate production in Beijing haze. *Atmos. Chem. Phys.* **18**, 5515-5528 (2018).
20. H.-M. Hung, M.-N. Hsu, M. R. Hoffmann, Quantification of SO2 Oxidation on Interfacial Surfaces of Acidic Micro-Droplets: Implication for Ambient Sulfate Formation. *Environ. Sci. Technol.* **52**,

9079-9086 (2018).

21. H.-M. Hung, M. R. Hoffmann, Oxidation of Gas-Phase SO2 on the Surfaces of Acidic Microdroplets: Implications for Sulfate and Sulfate Radical Anion Formation in the Atmospheric Liquid Phase. *Environ. Sci. Technol.* **49**, 13768-13776 (2015).

22. S. Song *et al.*, Possible heterogeneous chemistry of hydroxymethanesulfonate (HMS) in northern China winter haze. *Atmos. Chem. Phys.* **19**, 1357-1371 (2019).

23. J. Shao *et al.*, Heterogeneous sulfate aerosol formation mechanisms during wintertime Chinese haze events: air quality model assessment using observations of sulfate oxygen isotopes in Beijing. *Atmos. Chem. Phys.* **19**, 6107-6123 (2019).

24. J. Xue *et al.*, Sulfate Formation Enhanced by a Cocktail of High NOx, SO2, Particulate Matter, and Droplet pH during Haze-Fog Events in Megacities in China: An Observation-Based Modeling Investigation. *Environ. Sci. Technol.* **50**, 7325-7334 (2016).

25. G. Wang *et al.*, Particle acidity and sulfate production during severe haze events in China cannot be reliably inferred by assuming a mixture of inorganic salts. *Atmos. Chem. Phys.* **18**, 10123-10132 (2018).

26. J. M. Moch *et al.*, Contribution of Hydroxymethane Sulfonate to Ambient Particulate Matter: A Potential Explanation for High Particulate Sulfur During Severe Winter Haze in Beijing. *Geophys. Res. Lett.* **45**, 11,969-911,979 (2018).

27. M. A. Freedman, E.-J. E. Ott, K. E. Marak, Role of pH in Aerosol Processes and Measurement Challenges. *J. Phys. Chem. A* **123**, 1275-1284 (2019).

28. J. H. Seinfeld, S. N. Pandis, *Atmospheric chemistry and physics: from air pollution to climate change* (John Wiley & Sons, 2016).

29. A. S. Wexler, S. L. Clegg, Atmospheric aerosol models for systems including the ions H+, NH4+, Na+, SO42−, NO3−, Cl−, Br−, and H2O. *J. Geophys. Res.-Atmos.* **107**, ACH 14-11-ACH 14-14 (2002).

30. E. A. E-AIM, Aerosol Thermodynamics Model. *Website URL: http://www. aim. env. uea. ac. uk/aim/aim. php*.

31. S. L. Clegg, J. H. Seinfeld, Thermodynamic Models of Aqueous Solutions Containing Inorganic Electrolytes and Dicarboxylic Acids at 298.15 K. 2. Systems Including Dissociation Equilibria. *J. Phys. Chem. A* **110**, 5718-5734 (2006).

32. M. D. Petters, S. M. Kreidenweis, A single parameter representation of hygroscopic growth and cloud condensation nucleus activity. *Atmos. Chem. Phys.* **7**, 1961-1971 (2007).

33. M. R. Canagaratna *et al.*, Chemical and microphysical characterization of ambient aerosols with the aerodyne aerosol mass spectrometer. *Mass Spectrom. Rev.* **26**, 185-222 (2007).

34. F. Maaß, H. Elias, K. J. Wannowius, Kinetics of the oxidation of hydrogen sulfite by hydrogen peroxide in aqueous solution:: ionic strength effects and temperature dependence. *Atmos. Environ.* **33**, 4413-4419 (1999).

35. J. V. McArdle, M. R. Hoffmann, Kinetics and mechanism of the oxidation of aquated sulfur dioxide by hydrogen peroxide at low pH. *J. Phys. Chem* **87**, 5425-5429 (1983).

36. H. M. Ali, M. Iedema, X. Y. Yu, J. P. Cowin, Ionic strength dependence of the oxidation of SO2 by H2O2 in sodium chloride particles. *Atmos. Environ.* **89**, 731-738 (2014).

37. F. J. Millero, J. B. Hershey, G. Johnson, J.-Z. Zhang, The solubility of SO2 and the dissociation of H2SO3 in NaCl solutions. *J. Atmos. Chem.* **8**, 377-389 (1989).

38. S. Song *et al.*, Fine-particle pH for Beijing winter haze as inferred from different thermodynamic

equilibrium models. *Atmos. Chem. Phys.* **18**, 7423-7438 (2018).

39. M. Qin *et al.*, Impacts of heterogeneous reactions to atmospheric peroxides: Observations and budget analysis study. *Atmos. Environ.* **183**, 144-153 (2018).
40. J. B. Burkholder *et al.*, The Essential Role for Laboratory Studies in Atmospheric Chemistry. *Environ. Sci. Technol.* **51**, 2519-2528 (2017).
41. S. Wang *et al.*, Organic Peroxides and Sulfur Dioxide in Aerosol: Source of Particulate Sulfate. *Environ. Sci. Technol.* **53**, 10695-10704 (2019).
42. Y. Chen *et al.*, Response of the Aerodyne Aerosol Mass Spectrometer to Inorganic Sulfates and Organosulfur Compounds: Applications in Field and Laboratory Measurements. *Environ. Sci. Technol.* **53**, 5176-5186 (2019).
43. B. M. Matthew, A. M. Middlebrook, T. B. Onasch, Collection Efficiencies in an Aerodyne Aerosol Mass Spectrometer as a Function of Particle Phase for Laboratory Generated Aerosols. *Aerosol Sci. Technol.* **42**, 884-898 (2008).
44. T. E. Graedel, C. J. Weschler, Chemistry within aqueous atmospheric aerosols and raindrops. *Rev. Geophys.* **19**, 505-539 (1981).

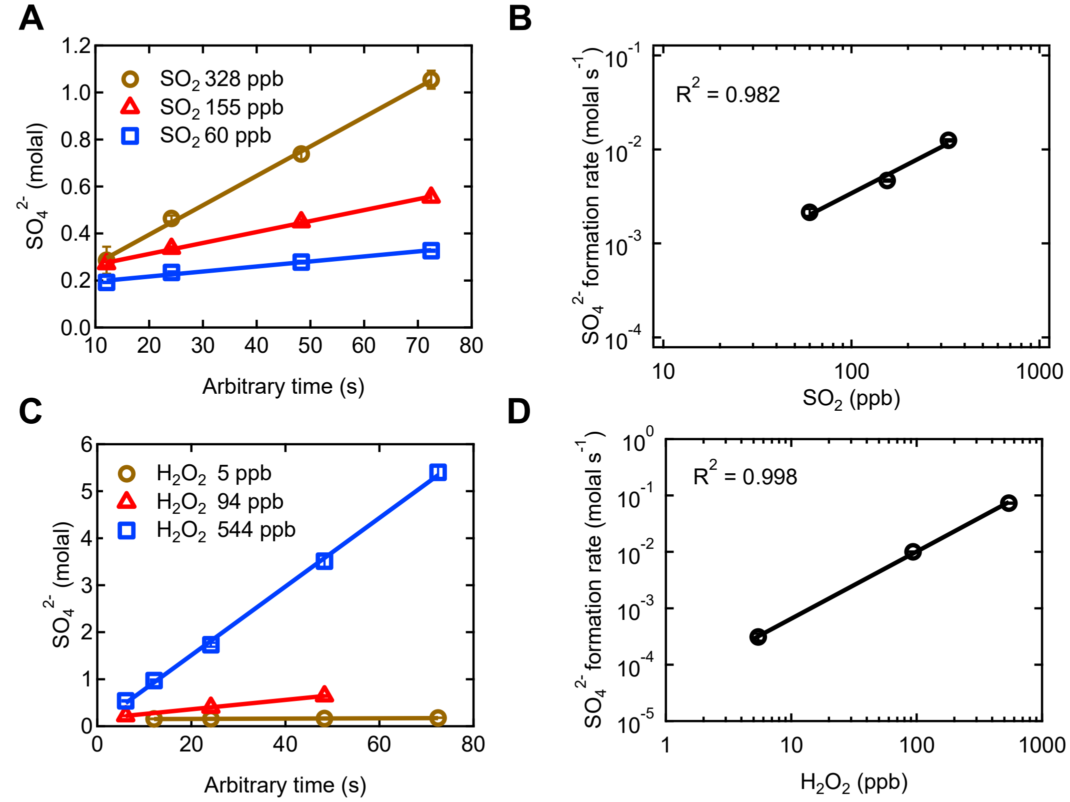

Fig. 1. Kinetics of aqueous oxidation of SO_2 by H_2O_2 in a mixture of NaCl and malonic acid buffer aerosol particles (molar ratio of 20:1:1) at pH 2.5. (A) Sulfate concentrations (units of molal) as a function of reaction time for initial SO_2 concentrations of 60, 155, and 328 ppb, for a H_2O_2 mixing ratio of 94 ppb (*SI Appendix*, Table S1, Exp 7 through 9). **(B)** Dependence of sulfate formation rate (molal s^{-1}) on initial SO_2 concentrations, for a H_2O_2 mixing ratio of 94 ppb. **(C)** Sulfate concentrations as a function of reaction time for initial H_2O_2 concentrations of 5, 94, and 544 ppb, for a SO_2 mixing ratio of 340 ppb (*SI Appendix*, Table S1, Exp 10 through 12). **(D)** Dependence of sulfate formation rate on initial H_2O_2 concentrations, for an SO_2 mixing ratio of 340 ppb. All error bars represent 1 SD; they are generally smaller than the symbol size.

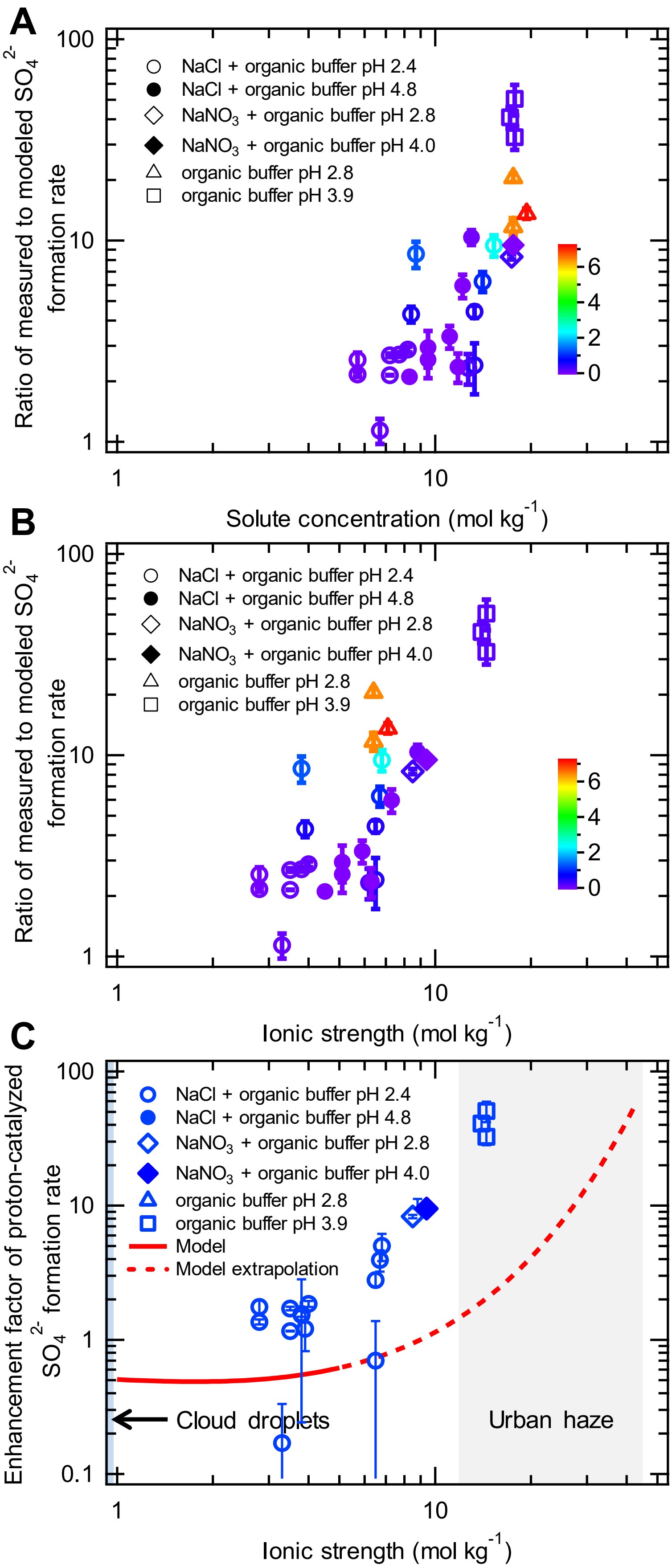
A
B
C
Ratio of measured to modeled SO_4^{2-} formation rate
Enhancement factor of proton-catalyzed SO_4^{2-} formation rate
100
10
1
0.1
NaCl + organic buffer pH 2.4
NaCl + organic buffer pH 4.8
$NaNO_3$ + organic buffer pH 2.8
$NaNO_3$ + organic buffer pH 4.0
organic buffer pH 2.8
organic buffer pH 3.9
Model
Model extrapolation
6
4
2
0
Cloud droplets
Urban haze
1
10
Solute concentration (mol kg^{-1})
Ionic strength (mol kg^{-1})
Ionic strength (mol kg^{-1})

Fig. 2. Ratio of the measured to modeled sulfate formation rates and enhancement factor of proton-catalyzed sulfate formation rate. (A) Dependence of the ratio of the measured to modeled sulfate formation rate on total solute concentration and malonic acid concentrations for a mixture of NaCl and organic buffer aerosol particles (circle symbols), $NaNO_3$ and organic buffer aerosol particles (rhombus symbols) and organic buffer aerosol particles at aerosol pH of 2.8 (triangle symbols) and 3.9 (square symbols). **(B)** Same as Fig. 2A but plotted against ionic strength. See *SI Appendix*, Fig. S4 for an equivalent plot where RH is indicated. **(C)** Dependence of the enhancement factor of proton-catalyzed sulfate formation rate on ionic strength. The calculated proton-catalyzed sulfate formation rates for organic buffer aerosol particles at aerosol pH of 2.8 and most data for the NaCl and organic buffer aerosol particles at aerosol pH of 4.8 were negative and so are not plotted. The model results (solid line) describe the effects of ionic strength on the proton-catalyzed sulfate formation rate measured in bulk solutions (34, 36, 37). The model extrapolation is shown as a dashed red line. Light blue– and gray–shaded areas indicate characteristic ionic strength ranges for cloud droplets and aerosol particles during urban haze episodes, respectively. All error bars are derived from the uncertainties of the measured sulfate formation rates.

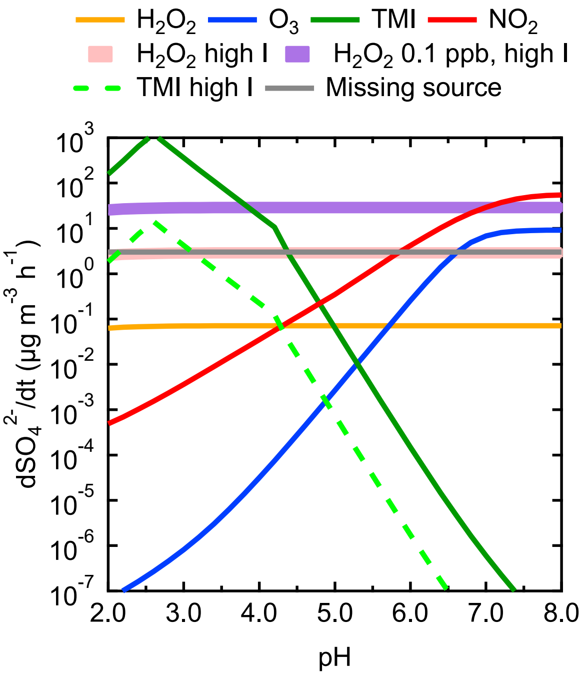

Fig. 3. Sulfate formation rates by aqueous SO_2 oxidation in aerosol particles under severe haze conditions. Colored solid lines represent sulfate formation rates calculated for different reaction pathways at conditions of: [SO_2 (g)] = 40 ppb, [H_2O_2 (g)] = 0.01 ppb, [NO_2 (g)] = 66 ppb, [O_3 (g)] = 1 ppb, pH-dependent concentrations of [Fe (III)] and [Mn (II)] (6), AWC = 300 µg m^{-3}, aerosol droplet radius $R_p = 0.15$ µm, T = 271 K, and $I = 0$ molal. The total soluble Fe and Mn are 18 and 42 ng m^{-3}, respectively. The Fe (III) concentration may be limited by the solubility of $Fe(OH)_3$ in which case the saturated concentration of Fe(III) was estimated from the solubility product equilibrium constant of $Fe(OH)_3$ ($K_{sp} = 2.6\times 10^{-38}$) (44). The pink-shaded area represents the sulfate formation rate for H_2O_2 reaction pathway accounting for the rate enhancement at $I = 14$ molal (and [H_2O_2 (g)] = 0.01 ppb). The purple-shaded area represents the sulfate formation rate for H_2O_2 reaction pathway at $I = 14$ molal and a higher concentration of [H_2O_2 (g)] = 0.1 ppb as observed during Beijing haze events (18). The dashed green line indicates the sulfate formation rate for TMI reaction pathway accounting for the impact of ionic strength. The grey line shows a missing sulfate formation rate of 3 µg m^{-3} $\cdot h^{-1}$ as a reference. This figure is constructed using the characteristic data conditions from ref. 6 along with additional components related to our analysis.

Supplementary Information for

Fast oxidation of sulfur dioxide by hydrogen peroxide in deliquesced aerosol particles

Tengyu Liu,[,1] Simon L. Clegg,[2] and Jonathan P. D. Abbatt*[,1]*
[1] Department of Chemistry, University of Toronto, Toronto, ON, M5S 3H6, Canada.
[2] School of Environmental Sciences, University of East Anglia, Norwich NR4 7TJ, U.K.

Tengyu Liu and Jonathan P. D. Abbatt
Email: tengyu.liu@utoronto.ca, jonathan.abbatt@utoronto.ca

This PDF file includes:

- Supplementary text
- Figures S1 to S10
- Tables S1 to S5
- SI References

Supplementary Information Text

1 Flow tube experiments and instrument operation

1.1 Flow tube experiments

A schematic of the experimental setup is shown in Fig. S1. All experiments were conducted in a vertically oriented pyrex flow tube (length 95 cm, inner diameter 6.2 cm) at a total flow rate of 1500 sccm at laminar flow conditions (Re ~34). The interior walls of the flow tube were coated with a thin layer of halocarbon wax to minimize the wall loss of SO_2 and H_2O_2. A constant output atomizer (TSI Aerosol Generator 3076), operated at a flow rate of 3 slpm, was used to generate pH-buffered polydisperse deliquesced aerosol particles from the following solutions: A. a mixture of NaCl/malonic acid/sodium bimalonate (10/0.5/0.5 mM, 3/0.5/0.5 mM, and 1/0.5/0.5 mM), B. NaCl/sodium bimalonate/sodium malonate (10/0.5/0.5 mM, 3/0.5/0.5 mM, and 1/0.5/0.5 mM), C. $NaNO_3$/malonic acid/sodium bimalonate (10/0.5/0.5 mM), D. $NaNO_3$/sodium bimalonate/sodium malonate (10/0.5/0.5 mM), E. malonic acid/sodium bimalonate (5/5 mM), and F. sodium bimalonate/sodium malonate (5/5 mM). The solutions were freshly prepared before each experiment. A fraction of the humidified aerosol flow was passed through a Kr-85 neutralizer (TSI Inc.) and mixed with a humidified N_2 flow and a dry SO_2 flow and then entered the kinetics flow tube from the side inlet perpendicular to the flow tube. The majority of the atomizer output went to the exhaust. The humidified N_2 flow was produced by bubbling N_2 gas (from liquid N_2) through MilliQ water. SO_2 was delivered by a flow of 10, 25, or 50 sccm from a cylinder (11 ppm in N_2, Linde) to achieve three different SO_2 concentrations in the flow tube. Three different gas-phase H_2O_2 mixing ratios were achieved by bubbling 10 sccm N_2 gas through an aqueous H_2O_2 solution (15% by weight) and 20 sccm N_2 gas through a 15% or 30% H_2O_2 solution. The H_2O_2 flow was introduced into the central portion of the humidified aerosol flow through a 3-mm O.D. PFA Teflon tube shielded with a 6-mm O.D. movable stainless steel injector tube that is inserted axially down the center of the flow tube, enabling variable reaction times. The flow was drawn down the flow tube by the pumping action of a scanning mobility particle sizer (SMPS), an aerosol mass spectrometer (AMS), an SO_2 monitor, and an additional pump. For supplementary experiments, an H_2O_2 monitor was connected instead of the pump to quantify the H_2O_2 concentrations in the absence of seed aerosols. All experiments were carried out at 21-25 ºC and RH of 73-90% (Table S1). RH was measured by an in-line digital hygrometer (Vaisala M170). The RH was controlled by adjusting the humidity of the humidified N_2 flow and kept constant to within ~1% over the course of an experiment. Note that all the H_2O_2/SO_2 experiments were conducted in N_2 carrier gas to minimize the potential for O_2 oxidation of the SO_2.

For each kinetics run, the aerosol particles were first characterized in the presence of SO_2 and the absence of H_2O_2 to quantify the background sulfate formation between the interaction of SO_2 and seed aerosols. Then the aqueous oxidation of SO_2 was initiated by introducing H_2O_2. The reaction time was adjusted by pushing the movable injector all the way in the flow tube in a stepwise manner from 60 cm to 10 cm away from the bottom. Reverse order of pulling the movable injector all the way out did not affect the sulfate formation rate. Fig. S2 shows the time series of RH, SO_2, particle volume, organics and sulfate concentrations for a typical experiment. As described above, the RH was stable over the course of the experiment. The sulfate concentration decreased with the decrease of the reaction time while the volumes of dry and wet aerosol particles remained relatively invariable. For the quantification of sulfate, the background sulfate signal was subtracted from the total steady-state sulfate concentrations. The contributions of background sulfate to the total steady-state sulfate concentrations were all less than 7%. For aerosol particles with only organic buffer present, the estimated buffer capacity (defined as the amount of H^+ needed to change the pH by 1 unit) can buffer 2.5 – 4.3 molal of H^+, which is typically higher than the amount of H^+ formed. However, for the particles containing NaCl or $NaNO_3$, the estimated buffer capacity is 0.1 – 1.3 molal of H^+, which is lower than the amount of H^+ formed for some data points. It is possible that HCl or HNO_3 evaporate from the particles under those conditions, removing acidity.

1.2 Instrument operation

Compact and high-resolution time-of-flight aerosol mass spectrometers (1) (C-ToF-AMS and HR-ToF-AMS; Aerodyne Research) were deployed to characterize the concentration and chemical composition of aerosol particles for experiments with and without NaCl present, respectively. The HR-ToF-AMS was operated in the high sensitivity V-mode with a time resolution of 1 minute. The toolkit Squirrel 1.60Q and Pika 1.20Q were used to analyze the AMS data. The concentration of sulfate ($\mu g\ m^{-3}$) was calculated by summing the nitrate-equivalent masses of each high-resolution ion associated with the sulfate fraction. The sulfate was measured in the form of sodium sulfate since the sulfuric acid that forms was buffered by sodium bimalonate or sodium malonate. For sodium sulfate, there is no pathway to produce water fragments after vaporization and ionization. Therefore, a sulfate fragmentation table without water fragments was used (2). Prior to the experiments, the ionization efficiency (IE) of the AMS was calibrated using 300 nm ammonium nitrate particles. The relative ionization efficiency (RIE) of sulfate was determined for sodium sulfate. Polydisperse pure sodium sulfate was atomized to the AMS and SMPS simultaneously. The sodium sulfate particles were passed through a diffusion dryer to remove aerosol water before they were sampled to the SMPS, while they were kept in the liquid phase without passing through a diffusion dryer prior to characterization by AMS, wherein the collection efficiency of particles was assumed to be unity (3). The particle size distributions measured by SMPS were converted to mass concentrations using the density of sodium sulfate of 2.68 g cm^{-3} (4), and converted to sulfate concentrations via the sulfate mass fraction of sodium sulfate. The RIE of sulfate was derived by comparing the sulfate concentrations measured by AMS and SMPS, determined to be 0.12 and 0.24 for C-ToF-AMS and HR-ToF-AMS, respectively. The higher RIE for HR-ToF-AMS is likely due to its higher vaporizer power of 5 Watt than that of 4.6 Watt for C-ToF-AMS. After applying the RIE calibration, the difference between sulfate concentrations simultaneously measured by these two AMS was within 10%.

The SMPS instrument consists of a differential mobility analyzer (DMA, TSI 3081) and a condensation particle counter (CPC, TSI 3772). The aerosol and sheath flow rates were 0.3 and 3 L min^{-1}, respectively, allowing for a size distribution scans ranging from 15–410 nm.

1.3 Choice of aerosol systems

The constraints for the experiment were to: i) work with aerosol components with variable hygroscopicity, to enable variations in solute strength, ii) have the ability to add pH buffers to the particles, iii) use aerosol particle solutions for which there are rigorous thermodynamic predictions of hygroscopicity and acidity, and iv) have the ability for sulfate yields to be accurately quantified with an aerosol mass spectrometer.

As a result, i) We chose to work with NaCl, $NaNO_3$, and organic acid particles, given their variable hygroscopicities. ii) To control the pH, we chose to use organic acid buffers given that the malonate/bimalonate/malonic acid system establishes pH values close to those of atmospheric aerosol. As well, organic acids are common urban aerosol constituents. iii) All of the individual components (chloride, sodium, nitrate malonate/bimalonate/malonic acid) are modelled by the E-AIM thermodynamic model, allowing for pH and ionic strength assessments. Note, for example, that we considered using phosphate pH buffers but they are not in E-AIM, nor are they atmospherically relevant. iv) These experiments cannot be conducted with an aerosol system largely composed of sulfate (e.g. $(NH_4)_2SO_4$) because sulfate is the reaction product, i.e. it is required to start with low sulfate mass loadings so that the formation of sulfate can be clearly observed during the reaction. Similarly, we could not use NH_4^+ as an initial component of the aerosol particles because the formation of $(NH_4)_2SO_4$ during the reaction would drastically change the sensitivity of the AMS to sulfate during the experiment (because the relative ionization efficiency of sulfate in $(NH_4)_2SO_4$ is very different from that of Na_2SO_4). In particular, as the reaction proceeded, a varying ratio of $(NH_4)_2SO_4$ to Na_2SO_4 would be formed. By only using Na^+ as the cation in the particles, we are fully confident that the reaction product is Na_2SO_4, which is a species for which the aerosol mass spectrometer can be calibrated. As well, by not using NH_4^+ as the cation, we avoid complications arising from NH_3 evaporation, with associated impacts on aerosol pH.

2 Modeled SO_4^{2-} formation rate

Modeled sulfate formation rates were calculated based on the literature parameters of aqueous SO_2 oxidation by H_2O_2 obtained in bulk solutions, without taking the effects of ionic strength and general acid catalysis into account. The rate expressions, rate coefficients and equilibrium constants that we used to calculate the aqueous-phase concentrations of SO_2 and H_2O_2 are shown in Tables S2 and S3, respectively. Note that we assume the sulfate formation rate in molal s^{-1} equals to that in M s^{-1} for the dilute solutions.

The modeled enhancement factors of sulfate formation rate in the main text Fig. 2C were calculated based on parameters obtained in bulk solutions (5-7) for ionic strength of 0-5 molal, accounting for the overall effects of ionic strength on the proton-catalyzed reaction rate coefficient *k*, Henry's law constants of H_2O_2 and SO_2, and the first stoichiometric dissociation constant of H_2SO_3. The effects of ionic strength on the reaction rate coefficient *k* and equilibrium constants are shown in Table S4 and Fig. S5. With the increase of ionic strength, the reaction rate coefficient *k* decreases first, followed by a minimum and then an increase while the first stoichiometric dissociation constant of H_2SO_3 shows a reverse trend. Increasing the ionic strengths, the Henry's law constants of H_2O_2 and SO_2 show trends of slight increase and decrease, respectively.

Also, we performed very preliminary calculations to assess how ionic strength in an ammonium sulfate particle may affect reactant concentrations, as compared to the results for NaCl and $NaNO_3$. The two Henry's law constants on the right hand side of Equation (1) of the main paper both involve uncharged solution species. The sulfate ion tends to have a salting-out effect relative to Na^+, Cl^- and NO_3^-, so it is expected that the stoichiometric values of H_{SO2} and H_{H2O2} are somewhat smaller in a largely SO_4^{2-} medium. However, the activity coefficients of such species generally vary less with the composition of the solution than do those of ions, consequently the salt effects on the dissociation constant K_{a1}^* are likely to be much larger. If it is assumed that the activity coefficients of H^+ and HSO_3^- have approximately the same values in aqueous $(NH_4)_2SO_4$ as H^+ and HSO_4^-, we calculate that the stoichiometric value of K_{a1}^* is increased by the following factors relative to its value in

NaCl: 21 (90% RH, $I_{NaCl} = 2.8$ mol kg^{-1}, $I_{(NH4)2SO4} = 9.2$ mol kg^{-1}) and 68 (80% RH, $I_{NaCl} = 5.1$ mol kg^{-1}, $I_{(NH4)2SO4} = 17.5$ mol kg^{-1}), i.e. this would lead to an enhancement effect in the kinetics. By contrast, calculations comparing $NaNO_3$ and NaCl media yield values similar to each other which is consistent with our experimental results. We neglected the activity coefficient of H_2SO_3 in these calculations, on the assumption that its variation across the different salt media would be much smaller than that of the product of the H^+ and HSO_3^- activity coefficients. Note that we cannot estimate what the ionic strength effects are for the rate constant in Equation (1) for sulfate solutions.

3 General acid catalysis

Fig. S6 shows that the measured sulfate formation rate increases with the increase of malonic acid concentration at relatively constant pH and ionic strengths (Exp# 13-18), providing clear evidence that malonic acid buffer catalyzes the aqueous oxidation of SO_2 by H_2O_2. The reaction rate coefficient of general acid catalysis k_{HX} has been found to be negatively correlated with the pKa* of acid (8) (Fig. S7B). Based on this relationship, $k_{\text{malonic acid}}$ is estimated to be 43 times higher than $k_{\text{bimalonate}}$, so the general acid catalysis induced by bimalonate can be neglected. The $k_{\text{malonic acid}}$ values for ionic strengths of 3.9 and 6.6 molal were then determined to be 5.61×10^5 and 1.32×10^5 molal^{-2} s^{-1} from Fig. S6. We linearly fit these two rate constants (Fig. S7A) as a function of ionic strength. The ionic strength-dependent general acid catalyzed sulfate formation rate was then calculated (using Equation 1 in the main text) and subtracted from the measured sulfate formation rate to determine the proton-catalyzed sulfate formation rate. The justification for decreasing values for $k_{\text{malonic acid}}$ as a function of ionic strength is that the pKa* of malonic acid increases with ionic strength for concentrated solutions (Fig. S7C). Fig. S7B demonstrates that larger values of the pKa* lead to smaller values of $k_{\text{malonic acid}}$.

4 TMI experiments

We also utilized the kinetics flow tube to investigate the effects of ionic strength on aqueous phase TMI catalyzed oxidation of dissolved SO_2 by O_2 in aerosol particles. The experimental conditions are shown in Table S5. The pH-buffered polydisperse deliquesced aerosol particles with three different concentrations of TMI were prepared by atomizing the following solutions: a mixture of NaCl/malonic acid/sodium bimalonate (10/0.5/0.5 mM) with 1 μM iron (III) chloride ($FeCl_3$) and 50 μM, 0.2 mM, and 2 mM manganese (II) chloride ($MnCl_2$), respectively. All experiments were conducted at pH of 2.8 to ensure high solubility of Fe (III). Unlike the H_2O_2 experiments, the SO_2 flow for TMI experiments was introduced into the central portion of the humidified aerosol flow through the movable stainless steel tube, enabling variable reaction time. For an experimental run, the aerosol particles were first characterized in the absence of SO_2 to quantify the background sulfate in the seed aerosols. Then the aqueous oxidation of SO_2 was initiated by introducing SO_2. The TMI experiments were conducted in air as a carrier gas, given that O_2 is the oxidant.

Modeled sulfate formation rates were calculated based on the literature parameters of aqueous SO_2 oxidation by TMI+O_2 obtained in bulk solutions, without taking the effects of ionic strength into account. The relevant rate expressions, rate coefficients and equilibrium constants that we used to calculate the aqueous-phase concentrations of SO_2 are shown in Tables S2 and S3, respectively. Regarding the calculation of Fe (III) and Mn (II) concentrations in the aerosol particles, the molality of NaCl in the aerosol particles was first estimated using the E-AIM model (9). The Fe (III) and Mn (II) aerosols were expected to undergo the same degree of concentration after atomization. The molality of Fe (III) and Mn (II) was then estimated from the NaCl molality accordingly. The Fe (III) concentration may be limited by the solubility of $Fe(OH)_3$ in which case the saturated concentration of Fe (III) was estimated from the solubility product equilibrium constant of $Fe(OH)_3$ ($K_{sp} = 2.6\times 10^{-38}$) (10). Table S5 shows a comparison between the measured and modeled sulfate formation rates for the TMI experiments. We find that the sulfate formation rate for TMI oxidation decreases by a factor of approximately 85 at an ionic strength of 2.8 molal compared to that calculated for the dilute solution. The effect of ionic strength can be well described by the extended Debye-Hückel equation (Fig. S8) (11, 12). The fitting parameter of -3.02 is within the range of -2 for Fe (III) and -4 for Mn (II) (11, 12). In the main paper Fig. 3, we note that we likely overestimate the sulfate formation rate that will prevail for the TMI oxidation pathway at high ionic strength by using the inhibition factor obtained at a lower ionic strength of 2.8 molal.

5 Uncertainties of aerosol pH and aerosol liquid water volume

Fig. S9 shows a comparison of aerosol pH for the mixture of NaCl and organic buffer estimated using the E-AIM and Pitzer models. The Pitzer model gave approximately 0.4 unit lower pH values for the mixture of NaCl/malonic acid/sodium bimalonate and 1 unit higher pH values for the mixture of NaCl/sodium bimalonate/sodium malonate compared to the E-AIM model results. The enhancement factors for the proton-catalyzed sulfate formation rate at the highest ionic strength (~14 molal) remain unchanged when the E-AIM aerosol pH was used for the calculation (Fig. S10A). Therefore, the aerosol pH differences between the E-AIM and Pitzer models will not impact our conclusions.

We also determined the aerosol liquid water volume by multiplying the total measured aerosol volume by the ratio of the aerosol liquid water volume to the total aerosol volume estimated using the E-AIM model. The estimated aerosol liquid water volume is 1.0–1.9, 3.2–3.4, 2.9–4.9, and 1.7–2.0 times higher than the measured aerosol liquid water volume for the mixture of NaCl and organic buffer, $NaNO_3$ and organic buffer, organic buffer at pH 2.8, and organic buffer at pH 3.9, respectively. Consequently, the enhancement factor for the proton-catalyzed sulfate formation rate at ionic strengths of 14 molal decreases to 19 ± 3 – 30 ± 5 (Fig. S10B). The sulfate formation rate for the H_2O_2 reaction pathway in the main paper Fig. 3 will be lowered to 13.5–21.3 μg m^{-3} h^{-1}, remaining larger than the sulfate formation rates from other pathways. Therefore, using the estimated aerosol liquid water volume in the calculation will not impact our conclusion that the oxidation of SO_2 by H_2O_2 in aerosol particles can contribute to the missing sulfate source during severe haze episodes.

6 References

1. M. R. Canagaratna *et al.*, Chemical and microphysical characterization of ambient aerosols with the aerodyne aerosol mass spectrometer. *Mass Spectrom. Rev.* **26**, 185-222 (2007).
2. Y. Chen *et al.*, Response of the Aerodyne Aerosol Mass Spectrometer to Inorganic Sulfates and Organosulfur Compounds: Applications in Field and Laboratory Measurements. *Environ. Sci. Technol.* **53**, 5176-5186 (2019).
3. B. M. Matthew, A. M. Middlebrook, T. B. Onasch, Collection Efficiencies in an Aerodyne Aerosol Mass Spectrometer as a Function of Particle Phase for Laboratory Generated Aerosols. *Aerosol Sci. Technol.* **42**, 884-898 (2008).
4. I. N. Tang, H. R. Munkelwitz, Composition and temperature dependence of the deliquescence properties of hygroscopic aerosols. *Atmos. Environ.* **27**, 467-473 (1993).
5. F. J. Millero, J. B. Hershey, G. Johnson, J.-Z. Zhang, The solubility of SO2 and the dissociation of H2SO3 in NaCl solutions. *J. Atmos. Chem.* **8**, 377-389 (1989).
6. F. Maaß, H. Elias, K. J. Wannowius, Kinetics of the oxidation of hydrogen sulfite by hydrogen peroxide in aqueous solution:: ionic strength effects and temperature dependence. *Atmos. Environ.* **33**, 4413-4419 (1999).
7. H. M. Ali, M. Iedema, X. Y. Yu, J. P. Cowin, Ionic strength dependence of the oxidation of SO2 by H2O2 in sodium chloride particles. *Atmos. Environ.* **89**, 731-738 (2014).
8. C. Drexler, H. Elias, B. Fecher, K. J. Wannowius, Kinetic investigation of sulfur(IV) oxidation by peroxo compounds R-OOH in aqueous solution. *Fresenius J. Anal. Chem.* **340**, 605-615 (1991).
9. A. S. Wexler, S. L. Clegg, Atmospheric aerosol models for systems including the ions H+, NH4+, Na+, SO42−, NO3−, Cl−, Br−, and H2O. *J. Geophys. Res.-Atmos.* **107**, ACH 14-11-ACH 14-14 (2002).
10. T. E. Graedel, C. J. Weschler, Chemistry within aqueous atmospheric aerosols and raindrops. *Rev. Geophys.* **19**, 505-539 (1981).
11. L. Robbin Martin, M. W. Hill, The effect of ionic strength on the manganese catalyzed oxidation of sulfur(IV). *Atmos. Environ.* **21**, 2267-2270 (1987).
12. L. R. Martin, M. W. Hill, The iron catalyzed oxidation of sulfur: Reconciliation of the literature rates. *Atmos. Environ.* **21**, 1487-1490 (1987).
13. M. R. Hoffmann, J. G. Calvert, Chemical Transformation Modules for Eulerian Acid Deposition Models: Volume II, the Aqueous-phase Chemistry. *EPA/600/3-85* **17** (1985).
14. T. Ibusuki, K. Takeuchi, Sulfur dioxide oxidation by oxygen catalyzed by mixtures of manganese(II) and iron(III) in aqueous solutions at environmental reaction conditions. *Atmos. Environ.* **21**, 1555-1560 (1987).
15. J. H. Seinfeld, S. N. Pandis, *Atmospheric chemistry and physics: from air pollution to climate change* (John Wiley & Sons, 2016).
16. R. M. Kettler, D. J. Wesolowski, D. A. Palmer, Dissociation quotients of malonic acid in aqueous sodium chloride media to 100°C. *J. Solution Chem.* **21**, 883-900 (1992).

Table S1. SO_2/H_2O_2 experimental conditions and results.

Exp #	Aerosol type [a]	RH (%)	T (°C)	SO_2 (ppb)	H_2O_2 (ppb)	Aerosol pH [b]	Ionic strength (molal)	Malonic acid (molal)	Bimalonate (molal)	Measured SO_4^{2-} formation rate (molal s^{-1})	Modeled SO_4^{2-} formation rate (molal s^{-1})[c]	Calculated proton-catalyzed SO_4^{2-} formation rate (molal s^{-1})[d]
1	A1	74	23	341	94	2.3	6.5	0.547	0.368	0.0112	0.0047	0.0033
2	A1	75	23	347	94	2.3	6.2	0.330	0.224	0.0107	0.0046	
3	B1	78	21	348	94	4.8	6.3	0.027	0.207	0.0129	0.0055	
4	B1	83	22	343	94	4.8	5.1	0.017	0.176	0.0149	0.0051	
5	B1	82	22	343	94	4.8	5.1	0.017	0.176	0.0124	0.0048	
6	B1	86	22	343	94	4.8	4.5	0.013	0.159	0.0101	0.0048	
7	A1	86	22	328	94	2.4	3.8	0.190	0.155	0.0125	0.0046	0.0072
8	A1	90	22	60	94	2.5	2.8	0.137	0.121	0.0021	0.0008	0.0015
9	A1	89	22	155	94	2.5	2.8	0.137	0.121	0.0047	0.0022	0.0029
10	A1	88	22	340	5	2.5	3.3	0.164	0.139	0.00031	0.00027	0.00005
11	A1	87	22	340	544	2.5	3.5	0.177	0.147	0.0730	0.0271	0.0463
12	A1	87	22	340	94	2.5	3.5	0.177	0.147	0.0100	0.0047	0.0054
13	A1	74	23	345	94	2.3	6.5	0.547	0.368	0.0197	0.0044	0.0124
14	A2	73	24	345	94	2.3	6.7	1.060	0.705	0.0272	0.0043	0.0171
15	A3	73	24	345	94	2.3	6.8	2.452	1.664	0.0409	0.0043	0.0217
16	A1	85	25	316	94	2.4	4.0	0.203	0.163	0.0103	0.0036	0.0066
17	A2	85	24	316	94	2.4	3.9	0.595	0.480	0.0156	0.0036	0.0044
18	A3	85	25	316	94	2.4	3.8	1.326	1.083	0.0306	0.0036	0.0055
19	B1	79	24	350	94	4.8	5.9	0.024	0.198	0.0146	0.0044	
20	B2	78	24	350	94	4.8	7.3	0.068	0.584	0.0246	0.0041	
21	B3	78	24	350	94	4.8	8.8	0.121	1.207	0.0427	0.0041	0.0427
22	C	78	23	245	221	2.8	8.5	0.431	0.354	0.0616	0.0074	0.0616
23	D	78	23	245	221	4.0	9.4	0.024	0.343	0.0714	0.0075	0.0714
24	E	73	22	359	94	2.8	7.1	7.055	5.251	0.0683	0.0050	
25	F	74	22	359	94	3.9	14.5	0.256	3.043	0.1644	0.0050	0.1644
26	E	75	21	70	94	2.8	6.4	6.381	4.847	0.0225	0.0011	
27	E	75	21	179	94	2.8	6.4	6.381	4.847	0.0329	0.0028	
28	F	74	21	179	94	3.9	14.5	0.256	3.043	0.1426	0.0028	0.1426
29	E	75	23	349	94	2.8	6.4	6.381	4.847	0.0558	0.0047	
30	F	75	23	349	94	3.9	14.0	0.244	2.947	0.1958	0.0048	0.1958

[a] Six types of seed aerosols. A: NaCl/malonic acid/sodium bimalonate (A1: molar ratio of 20:1:1; A2: molar ratio of 6:1:1; A3: molar ratio of 2:1:1); B: NaCl/sodium bimalonate/sodium malonate (B1: molar ratio of 20:1:1; B2: molar ratio of 6:1:1; B3: molar ratio of 2:1:1); C: $NaNO_3$/malonic acid/sodium bimalonate (molar ratio of 20:1:1); D: $NaNO_3$/sodium bimalonate/sodium malonate (molar ratio of 20:1:1); E: malonic acid/sodium bimalonate (molar ratio of 1:1); F: sodium bimalonate/sodium malonate (molar ratio of 1:1).

[b] Aerosol pH of type A and B was estimated using the Pitzer model; C, D, E and F was estimated using the E-AIM model.

[c] Modeled sulfate formation rates were calculated based on the literature parameters of aqueous SO_2 oxidation by H_2O_2 obtained in bulk solutions, without taking the effects of ionic strength and general acid catalysis into account.

[d] The calculated proton-catalyzed sulfate formation rates were determined by subtracting the general acid catalyzed sulfate formation rate from the measured sulfate formation rate. For experiments 2-6, 19, 20, 24, 26, 27, and 29, the measured sulfate formation rates were lower than the estimated general acid catalysis sulfate formation rates; therefore, the calculated proton-catalyzed sulfate formation rates for these experiments were negative and not presented.

Table S2. Aqueous reactions rate expressions and rate coefficients.

Oxidants	Sulfate formation rate (molal s^{-1})	Reference
H_2O_2	$k'[H^+][HSO_3^-][H_2O_2(aq)]/(1+K[H^+])$ $k' = 7.45\times10^7\times e^{(-4430\times(1/T-1/298))}$ M^{-2} s^{-1} $K = 13$ M^{-1}	Hoffmann and Calvert (13)
$TMI+O_2$	$k_2[H^+]^{-0.74}[S(IV)][Mn(II)][Fe(III)]$ ($pH \leq 4.2$) $k_2 = 3.72\times10^7$ M^{-2} s^{-1} $k_3[H^+]^{0.67}[S(IV)][Mn(II)][Fe(III)]$ ($pH > 4.2$) $k_3 = 2.51\times10^{13}$ M^{-2} s^{-1}	Ibusuki and Takeuchi (14)

Table S3. Equilibrium constants for calculating aqueous-phase concentrations.

Species	Aqueous-phase concentration expressions	Equilibrium constants[a]	References
SO_2	$[H_2SO_3]=H_{SO_2}\times p_{SO_2}$	$H_{SO_2}=1.23\times e^{(3145.3\times(\frac{1}{T}-\frac{1}{298}))}$	Seinfeld and Pandis (15)
	$[HSO_3^-]=K_{a1}\times[H_2SO_3]/[H^+]$	$K_{a1}=1.3\times10^{-2}\times e^{(1960\times((\frac{1}{T}-\frac{1}{298}))}$	
	$[SO_3^{2-}]=K_{a2}\times[HSO_3^-]/[H^+]$	$K_{a2}=6.6\times10^{-8}\times e^{(1500\times((\frac{1}{T}-\frac{1}{298}))}$	
H_2O_2	$[H_2O_2(aq)]=H_{H_2O_2}\times p_{H_2O_2}$	$H_{H_2O_2}=1.3\times10^5\times e^{(7297.1\times(\frac{1}{T}-\frac{1}{298}))}$	Seinfeld and Pandis (15)

[a] H and K_a are in units of M atm^{-1} and M, respectively.

Table S4. Ionic strength (*I*) effects on aqueous reaction rate coefficient and equilibrium constants.

Parameter	Expressions	Notes	References
	$\frac{dSO_4^{2-}}{dt}=(k + k_{HX}\ [HX][H^+]^{-1})K_{a1}^*H_{SO_2}P_{SO_2}H_{H_2O_2}P_{H_2O_2}$		
k	$\log(\frac{k}{k^{I=0}})=0.36I-\frac{1.018\sqrt{I}}{1+0.17\sqrt{I}}$	I_{max} = 5 molal	Maaβ et al. (6)
$H_{H_2O_2}$	$\frac{H_{H_2O_2}}{H_{H_2O_2}^{I=0}}=1-1.414\times10^{-3}I^2+0.121I$	I_{max} = 5 molal	Ali et al. (7)
H_{SO_2}	$\log(\frac{H_{SO_2}}{H_{SO_2}^{I=0}})=(\frac{22.3}{T}-0.0997)\times I$	I_{max} = 6 molal	Millero et al. (5)
K_{a1}^*	$\log(\frac{K_{a1}^*}{K_{a1}^{I=0}})=0.5\times\sqrt{I}-0.31\times I$	I_{max} = 6 molal	Millero et al. (5)
K_{a2}^*	$\log(\frac{K_{a2}^*}{K_{a2}^{I=0}})=1.052\times\sqrt{I}-0.36\times I$	I_{max} = 6 molal	Millero et al. (5)

Table S5. SO_2/TMI experimental conditions and results.

Exp #	Aerosol type [a]	RH (%)	T (ºC)	SO_2 (ppb)	Aerosol pH	Fe (III) (mmolal) [b]	Mn (II) (mmolal) [b]	Ionic strength (molal)	Measured SO_4^{2-} formation rate (molal s^{-1})	Modeled SO_4^{2-} formation rate (molal s^{-1})
31	G	92	22	316	2.8	0.194 [c]	11.5	2.34	0.000621	0.046
32	H	94	22	307	2.8	0.176	352	2.82	0.015	1.277
33	I	94	24	292	2.8	0.176	35.2	1.87	0.0024	0.109

[a] Three types of seed aerosols. G: NaCl/malonic acid/sodium bimalonate/$FeCl_3$/$MnCl_2$ (10/0.5/0.5/0.001/0.05 mM) in atomizer solution; H: NaCl/malonic acid/sodium bimalonate/$FeCl_3$/$MnCl_2$ (10/0.5/0.5/0.001/2 mM) in atomizer solution; I: NaCl/malonic acid/sodium bimalonate/$FeCl_3$/$MnCl_2$ (10/0.5/0.5/0.001/0.2 mM) in atomizer solution.

[b] For each experiment, the molality of NaCl in the aerosol particles was first estimated using E-AIM model (9). The Fe (III) and Mn (II) aerosols were expected to undergo the same degree of concentration after atomization. The molality of Fe (III) and Mn (II) was then estimated from the NaCl molality accordingly.

[c] The Fe (III) concentration may be limited by the solubility of Fe $(OH)_3$ for Exp # 31. The saturated concentration of Fe (III) was estimated from the precipitation equilibrium of Fe $(OH)_3$ ($K_{sp} = 2.6\times 10^{-38}$) (10).

329

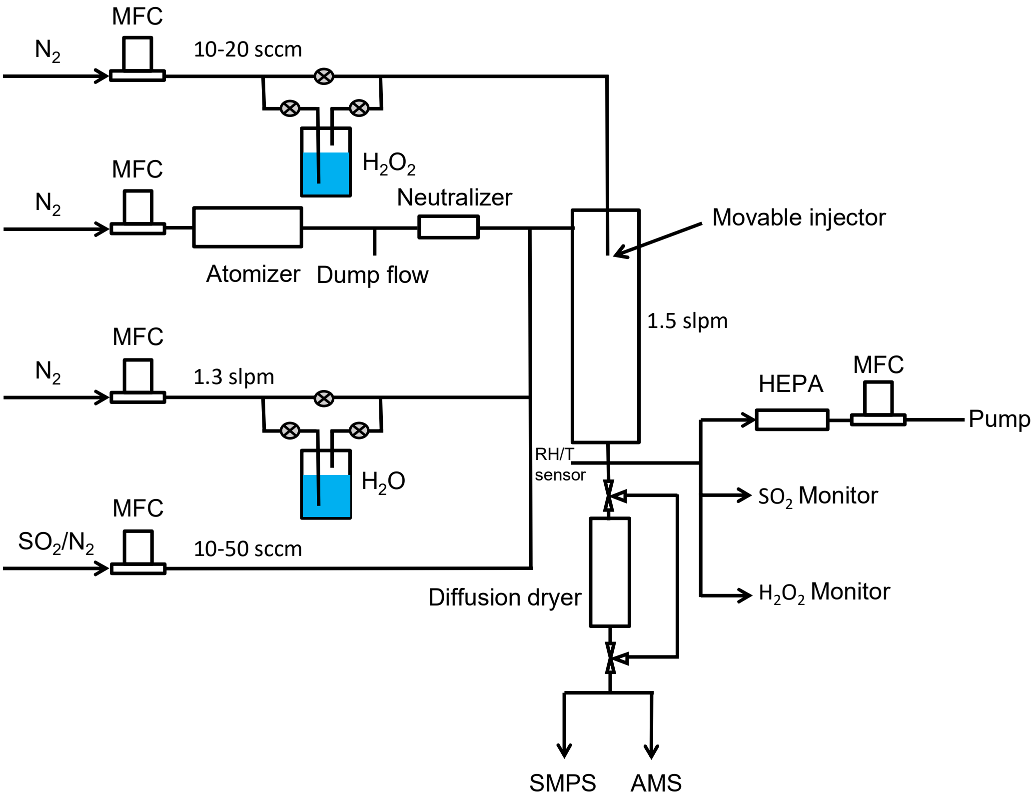

330 **Fig. S1.** Schematic of the experimental setup.

331

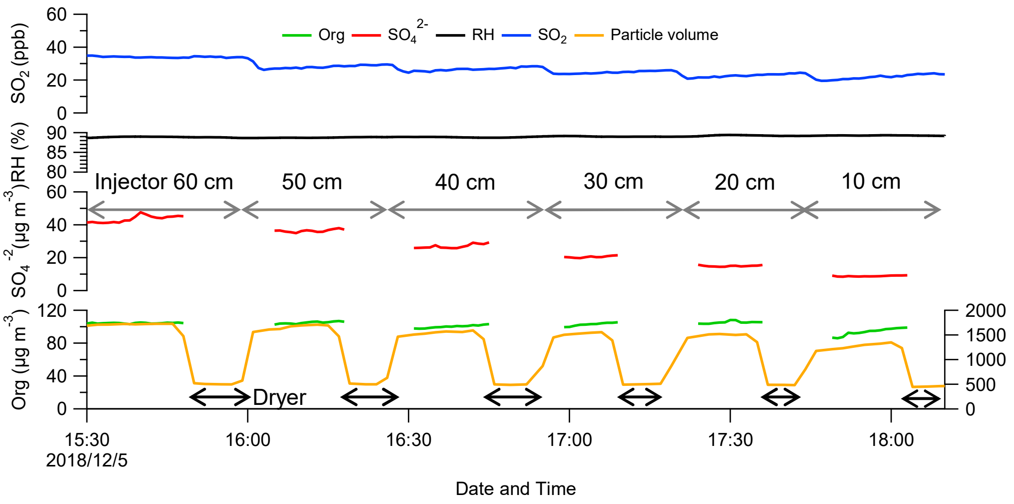

Fig. S2. Time series of RH, SO_2, particle volume, organics and sulfate concentrations for an experiment during which the aerosol water content was measured at each position, showing that it remains stable. For most experiments, the AWC was only measured once during the experiment.

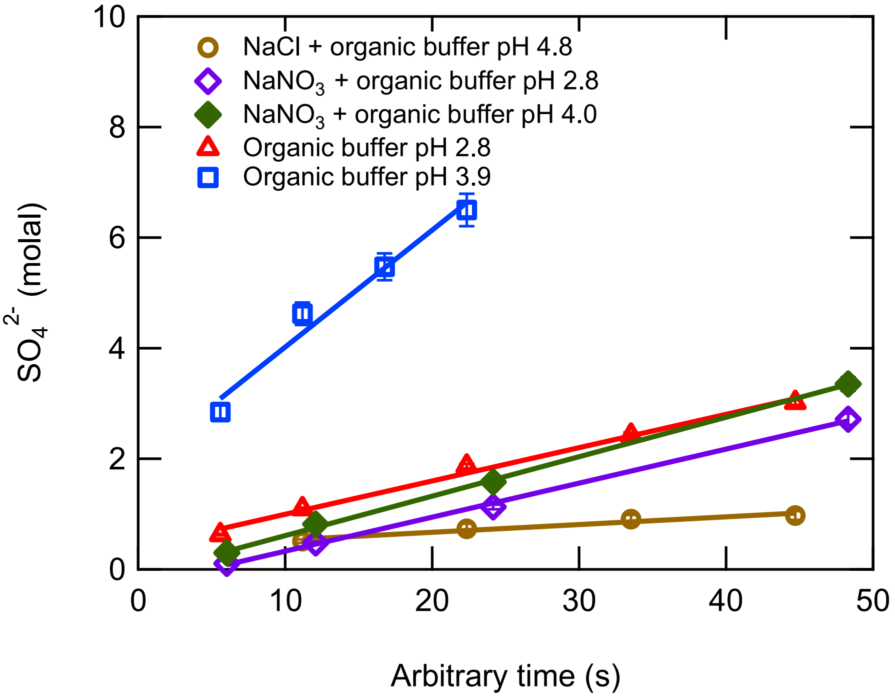

Fig. S3. Kinetics of aqueous oxidation of SO_2 by H_2O_2 in a mixture of NaCl and malonic acid buffer aerosol particles at pH 4.8 (Exp# 3), $NaNO_3$ and malonic acid buffer aerosol particles at pH 2.8 (Exp# 22) and pH 4.0 (Exp# 23), malonic acid buffer aerosol particles at pH 2.8 (Exp# 29) and 3.9 (Exp# 30).

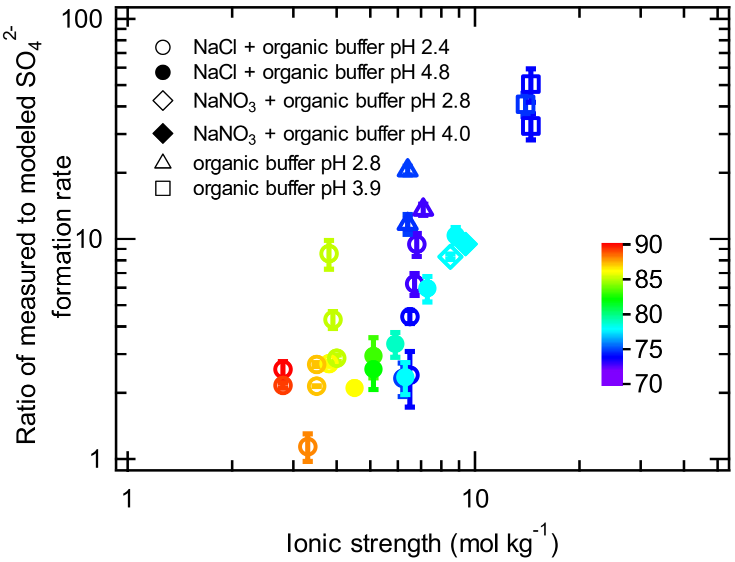

Fig. S4. Dependence of the ratio of the measured to modeled sulfate formation rate on ionic strength and RH.

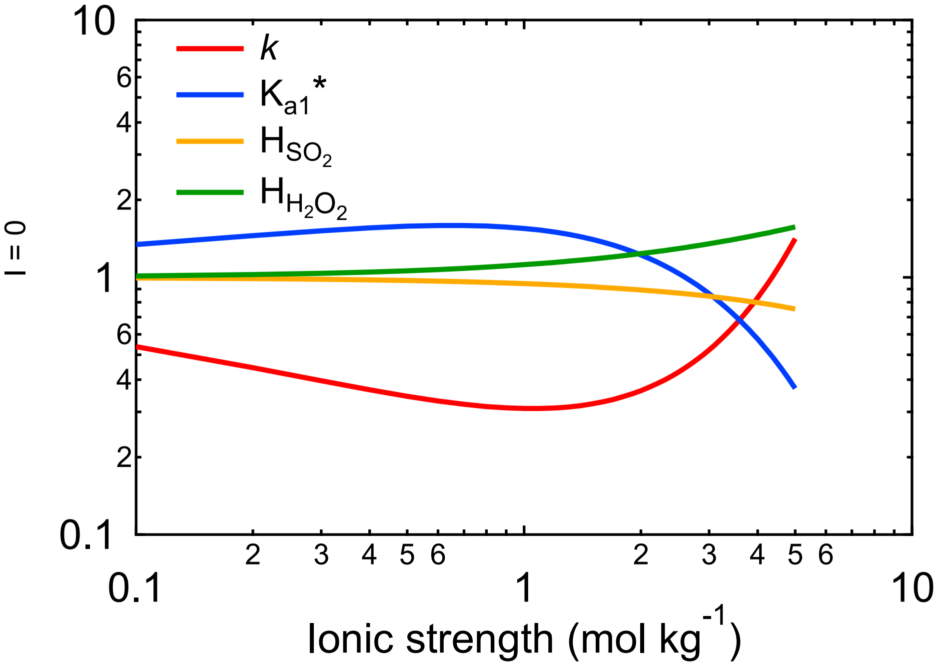

Fig. S5. Effects of ionic strength on aqueous reaction rate coefficient and stoichiometric equilibrium constants for the SO_2-H_2O_2 reaction. The parameter p represents the reaction rate coefficient or equilibrium constants.

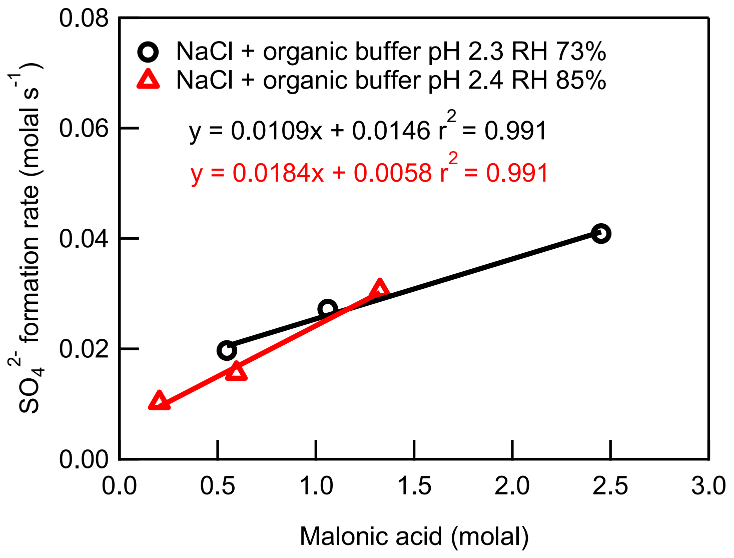

Fig. S6. Plot of sulfate formation rate as a function of malonic acid concentration for a mixture of NaCl and malonic acid buffer aerosol particles at pH 2.3 at RH of 73% (I = 6.6 molal, Exp# 13-15) and pH 2.4 at RH of 85% (I = 3.9 molal, Exp# 16-18).

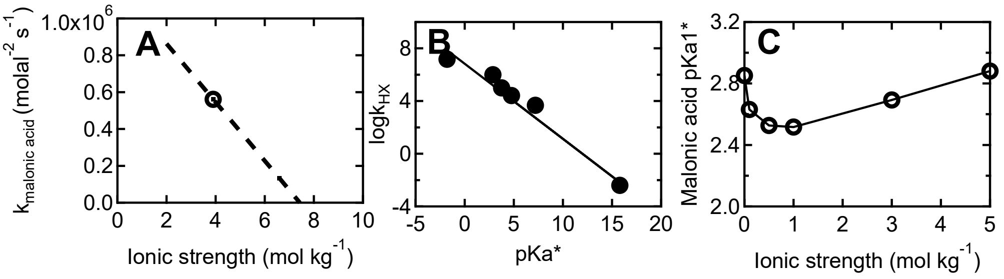

Fig. S7 (A) Dependence of $k_{\mathrm{malonic\ acid}}$ on the ionic strength. The $k_{\mathrm{malonic\ acid}}$ data for ion strengths of 3.9 and 6.6 molal were determined from Fig. S6, using Equation (1) and the calculated molality of H^+. The fitting equation is $k_{\mathrm{malonic\ acid}} = -1.59\times10^5 I + 1.18\times10^6$ **(B)** Plot of log k_{HX} versus pKa* of acid HX at 285 K and ionic strength of 0.5 molal. This figure is adapted from Drexler et al. (8) and the units for k_{HX} are $M^{-2}\,s^{-1}$. The fitting equation is log k_{HX} = -0.57pKa* (HX) + 6.83. **(C)** Dependence of the first pKa* of malonic acid on the ionic strength. This figure is adapted from Kettler et al. (16).

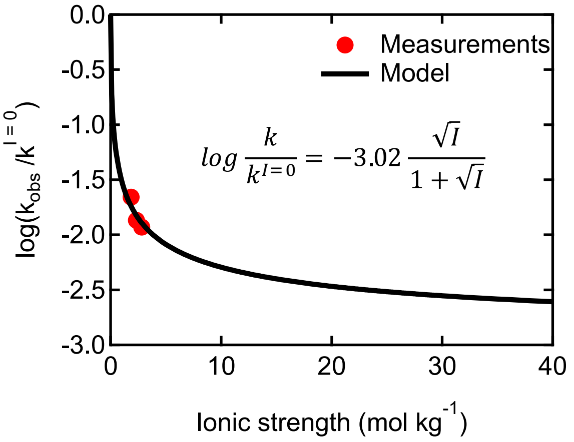

Fig. S8 Impact of ionic strength on the sulfate formation rate of aqueous phase TMI-catalyzed oxidation of dissolved SO_2 by O_2 in aerosol particles. The effect of ionic strength can be well described by the extended Debye-Hückel equation (11, 12), shown as an inset in the figure. The fitting parameter of -3.02 is within the range of -2 for Fe (III) and -4 for Mn (II) (11, 12).

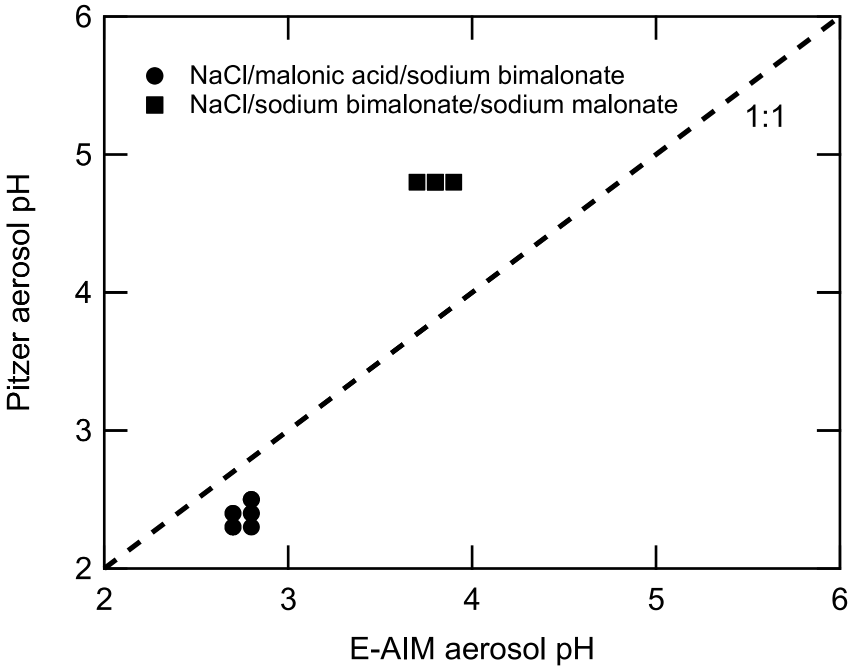

Fig. S9 Comparison of aerosol pH for the mixture of NaCl and organic buffer calculated using the Pitzer and E-AIM models.

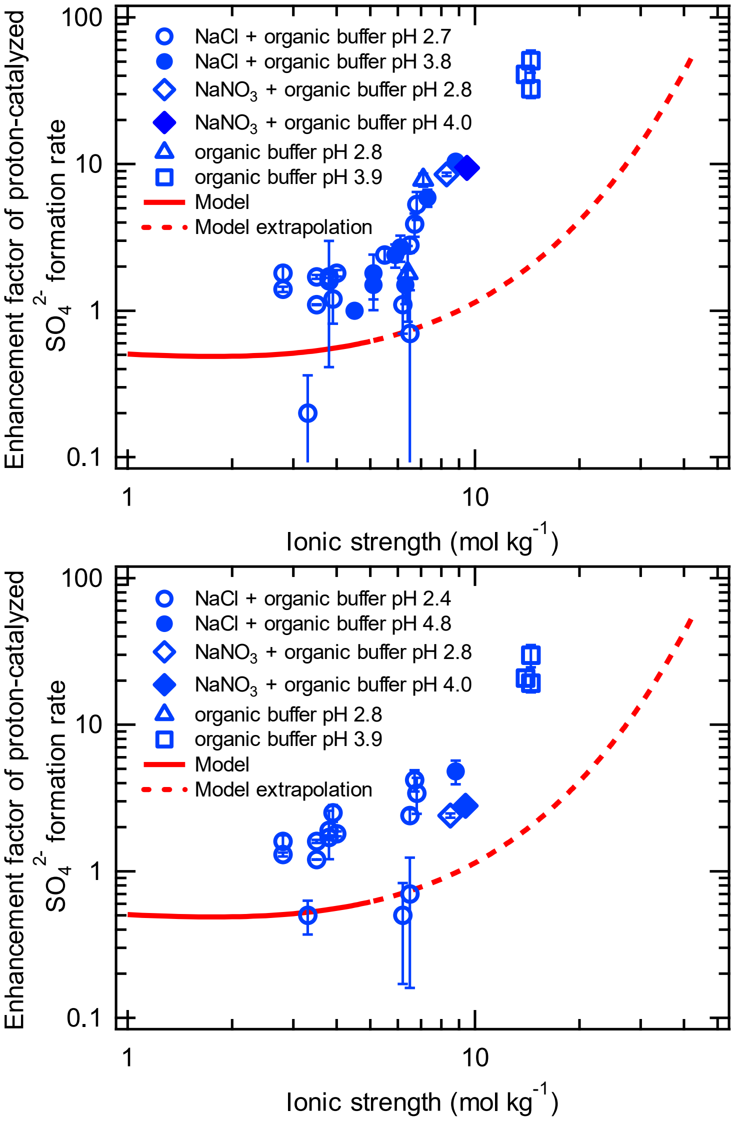

Fig. S10 Dependence of the enhancement factor of proton-catalyzed sulfate formation rate on ionic strength. **(A)** Aerosol pH for the mixture of NaCl and organic acid buffer was estimated using the E-AIM model. **(B)** Aerosol liquid water volume was determined by multiplying the total measured aerosol volume by the ratio of the aerosol liquid water volume to the total aerosol volume estimated using the E-AIM model.